ORIGINAL PAPER

CrossMark

Structure, electronic properties, and NBO and TD-DFT analyses of nickel(II), zinc(II), and palladium(II) complexes based on Schiff-base ligands

Amina Guelai[1] · Houari Brahim[1] · Abdelkrim Guendouzi[1] · Mostefa Boumediene[1] · Sefia Brahim[1]

Abstract

In this work we studied the structural and electronic properties of the metal–Schiff base complexes NiL_2^2 (**1**), PdL_2^1 (**2**), ZnL_2^2 (**3**), and NiL_2^1 (**4**), where L^1 and L^2 are Schiff bases synthesized from salicylaldehyde and 2-hydroxy-5-methylbenzaldehyde, respectively. Natural bond analysis showed that in complexes **1** and **2**, the metal ion coordinates to the ligands through electron donation from lone pairs on ligand nitrogen and oxygen atoms to s and d orbitals on the metal ion. In complex **3**, metal–N and metal–O bonds are formed through charge transfer from the lone pairs on nitrogen and oxygen atoms to an s orbital of Zn. Dimethylation of the phenolate rings in the ligands decreases the energy gap and redshifts the spectrum of the nickel complex. The main absorptions observed were assigned on the basis of singlet-state transitions. The simulated spectra of the two complexes **1** and **2** are characterized by excited states with ligand-to-ligand charge-transfer (LLCT), metal-to-ligand charge-transfer (MLCT), ligand-to-metal charge-transfer (LMCT), and metal-centered (MC) character.

Keywords TD-DFT · Schiff base · Complexes · Absorption spectrum · Nickel(II) · Zinc(II) · Palladium(II) · Excited states · NBO

Introduction

Schiff-base ligands are characterized by their ability to coordinate readily with various transition metal ions to form stable complexes that are easy to synthesize [1–3]. Often, the Schiff-base ligand has two or more electron-donating functional groups and can be coordinated with metal ions in different modes (monodentate, bidentate, tridentate, etc) via donor–acceptor interactions between the functional groups of the ligand and the metal [4]. Because of these remarkable properties, Schiff bases have become popular in a number of scientific fields, such as biological science and medicine [5]; indeed, metal–Schiff base complexes have been widely used as anti-

inflammatory and antibacterial agents [6–8]. To improve their biological activities, several studies aimed at synthesizing new allylamine-derived Schiff-base ligands and their respective complexes (usually with first-row metal ions) have been carried out [9–11]. Recently, a new class of such complexes has been synthesized: NiL_2^2 (**1**), PdL_2^1 (**2**), and ZnL_2^2 (**3**) (Fig. 1), where L^1 and L^2 are Schiff bases (L^1 = 2-allyliminomethyl phenolate and L^2 = 2-allyliminomethyl-4-methyl phenolate) synthesized from salicylaldehyde and 2-hydroxy-5-methylbenzaldehyde, respectively, as well as allylamine [12]. These three complexes have been fully characterized using different techniques and various spectroscopic methods of analysis. X-ray data show that complexes **1** and **2** adopt a square-planar geometry around the metallic ion and that complex **3** is nonplanar. In the UV-visible region, the three complexes are characterized by a weak band in the visible region and intense absorptions in the UV-C region. However, the geometric structures of the three complexes have not been well studied, particularly the first coordination sphere of the metal ion (or more precisely, how the metal ion coordinates with oxygen and nitrogen). In order to assign the main absorptions observed experimentally, the electronic absorption spectrum must be simulated. Numerous theoretical studies have

✉ Houari Brahim
brahim.h@outlook.com

1 Department of Chemistry, University of Saida—Docteur Moulay Tahar, 20000 Saida, Algeria

been carried out to study the geometric and electronic properties of Schiff base ligands and Schiff base–transition metal complexes [13–15]. Those works provide additional and indispensable support to experimental investigations, allowing more detailed study.

The objective of the work reported in the present paper was to theoretically study the structural, electronic, and optical properties of the three complexes **1**, **2**, and **3** via density functional theory (DFT) and time-dependent density functional theory (TD-DFT) calculations. We also studied the optical properties of the complex NiL_2^1 (**4**) in order to examine how dimethylation of the phenolate rings in the ligands affects the optical properties of the nickel complex.

Computational details

Geometry optimization calculations for complexes **1–3** were performed using density functional theory (DFT). This was achieved using the two hybrid functionals B3LYP [16–18] and mPW1PW91 [19] as well as the basis set 6-31++G(d,p) [20–22] to describe all nonmetal atoms and the combined basis set–pseudopotential Lanl2DZ [23, 24] to describe the metal atoms. The effects of the solvent (methanol, ε = 32.613) were introduced implicitly in terms of the polarizable continuum model (PCM) [25, 26]. These methods were used because they performed well in our previous studies [27, 28]. Geometry optimizations were followed by vibrational frequency calculations to confirm that the optimized structures were real minima. The ground-state geometries obtained were used to perform natural bond analysis [29–33] using the NBO program [34] implemented in Gaussian [35]. The NBO interactions were visualized with Jmol [36] using the Jmol NBO Visualization Helper [37]. The lowest-lying excited singlet states in methanol (CH_3OH) were studied using the TD-DFT method at the same level of theory used to perform the optimizations. All calculations were carried out using the Gaussian program.

Results and discussion

Structural investigations

The main structural parameters of the three complexes NiL_2^2 (**1**), PdL_2^1 (**2**), and ZnL_2^2 (**3**) (Fig. 1) in methanol, as computed with mPW1PW91 and B3LYP, are reported in Table 1, together with the corresponding experimental values. Geometry optimization was performed at C_i symmetry for complexes **1** and **2** and without any constraint for complex **3**. Therefore, the two complexes **1** and **2** present a square-planar ligand configuration around the metal ions Pd(II) and Ni(II), and the geometric parameters of the two ligands are equal in **1** and **2**. The geometric parameters computed with B3LYP and mPW1PW91 were found to be in good agreement with the corresponding experimental values. The mPW1PW91 results agree better with the X-ray data than the B3LYP results do. All calculated M–O bond lengths in the three complexes are shorter than the M–N bond lengths, which shows that oxygen and nitrogen do not bind in a similar manner to the metal ion (see below). The four bond angles N–M–O in complexes **1** and **2** are slightly different from 90° (the usual angle seen for a square-planar complex), and the intra-ring bond angles O_1–M–N_1 and O_2–M–N_2 (91.9°) are clearly larger than the inter-ligand bond angles O_1–M–N_2 and O_2–M–N_1 (88.0°) due to the rigidity of the aromatic ring system. In contrast to complexes **1** and **2**, complex **3** tends to adopt a deformed tetrahedral geometry in which the aromatic rings of the two phenolates are non-coplanar (see the dihedral angle values in Table 1).

Wiberg bond indices (WBIs) were calculated to probe the nature of the metal–O and metal–N bonds in the three complexes (Table 2). The WBI of the metal–O bond is bigger than that of the metal–N one, indicating that the former is stronger than the latter, which explains why the M–O bond is shorter than the M–N bond. B3LYP and mPW1PW91 gave very similar WBIs, with both levels of theory indicating that the metal–N and metal–O bonds
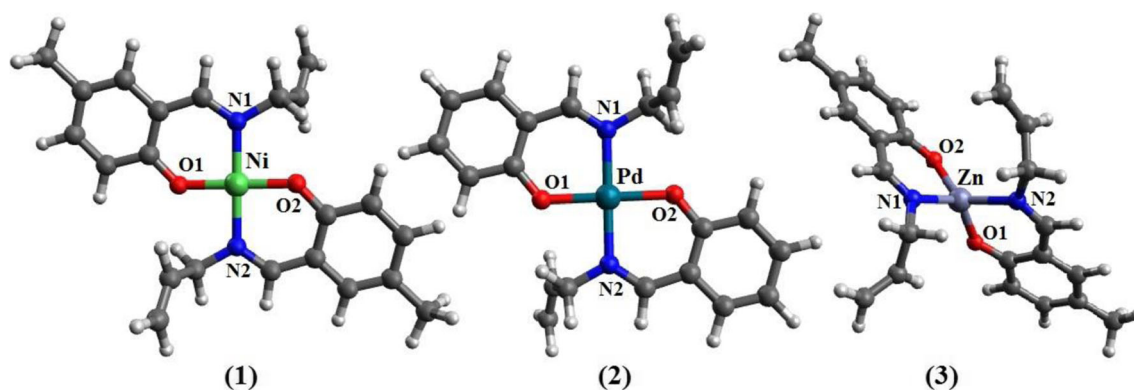

Fig. 1 The geometries of NiL_2^2 (**1**), PdL_2^1 (**2**), and ZnL_2^2 (**3**)

Table 1 Selected optimized and experimental bond lengths (in Å) and bond angles (in degrees) of the complexes NiL_2^2 (**1**), PdL_2^1 (**2**), and ZnL_2^2 (**3**)

	NiL_2^2 (**1**)			PdL_2^1 (**2**)			ZnL_2^2 (**3**)		
	B3LYP	mPW1PW91	X-ray	B3LYP	mPW1PW91	X-ray	B3LYP	mPW1PW91	X-ray
Bond lengths									
M–O_1	1.867	1.852	1.837	2.033	2.014	1.981	1.990	1.976	1.911
M–O_2	1.867	1.852	1.837	2.033	2.014	1.981	1.990	1.979	1.921
M–N_1	1.953	1.934	1.928	2.062	2.039	2.017	2.100	2.081	1.995
M–N_2	1.953	1.934	1.928	2.062	2.039	2.017	2.098	2.084	2.011
Bond angles									
O_1–M–N_1	91.9	92.0	92.5	88.9	88.7	88.0	91.8	91.9	97.0
O_2–M–N_2	91.9	92.0	92.5	88.9	88.7	88.0	132.1	132.2	120.2
O_1–M–N_2	88.0	87.9	87.4	91.0	91.2	91.9	129.1	128.5	117.4
O_2–M–N_1	88.0	87.9	87.4	91.0	91.2	91.9	91.5	91.7	96.8
O_1–M–O_2	180.0	180.0	180.0	180.0	180.0	180.0	108.3	108.7	112.9
N_1–M–N_2	180.0	180.0	180.0	180.0	180.0	180.0	108.9	108.5	113.7
N_2–M–O_2–O_1	0.0	0.0	0.0	0.0	0.0	0.0	124.0	124.8	127.1
N_2–M–O_2–N_1	180.0	180.0	180.0	180.0	180.0	180.0	121.9	119.9	121.4
N_2–M–N_1–O_1	0.0	0.0	0.0	0.0	0.0	0.0	123.8	124.2	127.3

are only weakly covalent. Weakly covalent metal–O and metal–N bonds have also been observed for other similar complexes [38]. The natural atomic charges (NACs), natural electron configurations (NECs), and total natural populations (core + valence + Rydberg) of the oxygen, nitrogen, and metal atoms/ions in the complexes, as obtained from NBO calculations, are reported in Table 2. The NECs of the Ni and Pd ions in the corresponding complexes are $4s^{0.31}3d^{8.63}$ and $5s^{0.33}4d^{8.75}$, respectively (note that we omitted the small contribution from the $4p$ and $5d6p$ orbitals), while the NEC of the free metal ion is $4s3d^8$ for Ni^{2+} and $5s4d^8$ for Pd^{2+}. Thus, upon

Table 2 The Wiberg bond indices (WBIs), natural atomic charges (NACs), total natural populations (TNPs, in parentheses), and natural electron configurations (NECs) of selected atoms/ions in complexes **1**–**3**, as calculated at the B3LYP and mPW1PW91 levels of theory

	NiL_2^2 (**1**)		PdL_2^1 (**2**)		ZnL_2^2 (**3**)	
	B3LYP	mPW1PW91	B3LYP	mPW1PW91	B3LYP	mPW1PW91
WBI						
M–O_1	0.354	0.349	0.364	0.358	0.133	0.128
M–O_2	0.354	0.349	0.364	0.358	0.131	0.122
M–N_1	0.344	0.341	0.361	0.366	0.128	0.119
M–N_2	0.344	0.341	0.361	0.366	0.127	0.116
NAC and (TNP)						
M	1.018 (26.98)	1.039 (26.96)	0.892 (45.10)	0.904 (45.09)	1.888 (28.30)	1.707 (28.29)
O	−0.757 (8.75)	−0.760 (8.76)	−0.727 (8.73)	−0.735 (8.73)	O_1: −0.879 O_2: −0.887	O_1: −0.882 O_2: −0.894
N	−0.521 (7.52)	−0.766 (7.52)	−0.493 (7.49)	−0.492 (7.49)	N_1: −0.688 N_2: −0.686	N_1: −0.690 N_2: −0.689

NEC (computed with mPW1PW91)

Ni[core]$4s^{0.31}3d^{8.63}4p^{0.02}$

Pd[core]$5s^{0.33}4d^{8.75}5d^{0.01}6p^{0.01}$

Zn[core]$4s^{0.29}3d^{9.98}4p^{0.03}$

complexation, electron density is donated from each ligand to a metal d orbital (significant donation) and from each ligand to a metal s orbital (low donation). Moreover, in complex **1**, the natural charges on Ni, O, and N are $+1.039e$, $-0.760e$, and $-0.766e$ instead of the expected $+2.0e$, $-2.0e$, and $-1.0e$, respectively. This result shows that electron transfer occurs from O and N orbitals to Ni orbitals. For the palladium complex, a similar interpretation of the NAC results shows that electron transfer occurs from O and N orbitals to Pd orbitals (Table 2). For complex **3**, the difference between the d-orbital occupancy of the zinc ion after complexation ($3d^{9.89}$) and that in the free ion ($3d^{10}$) is negligible. The s-orbital occupancy of Zn increases slightly when going from the free ion to the complex. Moreover, the natural charge on the Zn ion ($+2.0e$) does not change dramatically after complexation ($+1.707e$). Therefore, in complex **3**, electron transfer is weaker than in complexes **1** and **2**. The computed occupancies of the natural bond orbitals and their compositions in terms of natural atomic orbitals (NAOs) are given in Table S1 of the "Electronic supplementary material" (ESM). We focused on Lewis and non-Lewis NBOs that were associated with significant interaction energies. The calculated second-order interaction energy (E^2) of the strongest interactions between donor and acceptor orbitals are given in Table 3. Selected NBO–NBO* interactions are presented in Fig. 2 (complexes **1** and **3**) and Figure S1 of the ESM (complex **2**). As the two functionals give similar results in NBO analysis, we only provide the mPW1PW91 results here. Due to the symmetry

(C_i) of complexes **1** and **2**, the two ligands in each complex have the same NBO properties. The two lone pairs on the metal, LP*(1) and LP*(2) (non-Lewis NBOs), relate to the $d_{x^2-y^2}$ and $4s$ NAOs, respectively.

In complexes **1** and **2**, the metal ion coordinates to the nitrogen and oxygen atoms through electron donation from the lone pairs (LPs) on the nitrogen and oxygen atoms to the non-Lewis orbitals LP*(1) and LP*(2) of the metal ions (Table 3). The LP(1) of nitrogen and the LPs(1,2) of oxygen relate to the valence NAOs $2s$ and $2p$, whereas the LP*(1) and LP*(2) of the metal ions relate to $n(d_{x^2-y^2})$ and $n(s)$, respectively. The energies (E^2) of the interactions $(2s2p)N \rightarrow (d_{x^2-y^2})M$ and $(2s2p)N \rightarrow (s)M$ were estimated to be 43.12 and 45.47 kcal/mol for the nickel complex and 72.37 and 38.93 kcal/mol for the palladium complex, respectively. The strongest interaction between the metal ion and oxygen occurs through LP(3)O $\rightarrow (d_{x^2-y^2})M$ and LP(3)O $\rightarrow (s)M$ electron donation, which present significant energy values. The interactions $\pi_{C=C} \rightarrow \pi^*_{C=C}$ and LP(2,3)O $\rightarrow \pi^*_{C-C}$ are needed to form the aromatic rings of the ligands. In contrast to the Ni and Pd complexes, the d orbitals of the metal ion are not involved in the bonding of the Zn ion to N and O in complex **3**, because this complex adopts a tetrahedral symmetry (sp^3 hybridization). Instead, the Zn–N and Zn–O bonds result from charge transfer from LP(1)N and LP(1,2)O to an s orbital of Zn. The same donor $\rightarrow$ acceptor interaction has different energies for the three complexes due to differences between the complexes in the values of $F(i,j)$ (the Fock matrix element) and $E_j - E_i$ (acceptor $-$ donor NBO energies).

Table 3 Second-order perturbation energies E^2 (kcal/mol), off-diagonal NBO Fock matrix elements $F(i,j)$ (a.u.), and acceptor $-$ donor NBO energies ($E_j - E_i$) (a.u.) of selected donor–acceptor NBO interactions in complexes **1–3**, as calculated at the B3LYP and mPW1PW91 levels of theory

Donor—acceptor	NiL$_2^2$ (**1**)			PdL$_2^1$ (**2**)			ZnL$_2^2$ (**3**)		
	E^2	$E_j - E_i$	$F(i,j)$	E^2	$E_j - E_i$	$F(i,j)$	E^2	$E_j - E_i$	$F(i,j)$
LP(1)N$_{1,2}$—LP*(1)M	43.12	0.27	0.109	72.37	0.21	0.132			
LP(1)N$_{1,2}$—LP*(2)M	45.47	0.70	0.159	38.93	0.62	0.141	35.81 (35.04)[b]	0.63 (0.63)	0.140 (0.138)
LP(1)O$_{1,2}$—LP*(1)M	3.56	0.40	0.042	5.11	0.37	0.052			
LP(1)O$_{1,2}$—LP*(2)M	12.64	0.84	0.097	10.07	0.78	0.084	7.17 (7.18)	0.76 (0.76)	0.070 (0.070)
LP(2)O$_{1,2}$—LP*(1)M	17.47	0.16	0.055	5.57	0.05	0.019			
LP(2)O$_{1,2}$—LP*(2)M	16.03	0.59	0.088	1.45	0.46	0.023	31.65 (32.02)	0.63 (0.63)	0.133 (0.133)
LP(3)O$_{1,2}$—LP*(1)M	33.86	0.22	0.089	58.15	0.20	0.117			
LP(3)O$_{1,2}$—LP*(2)M	36.42	0.66	0.138	37.33	0.61	0.136			
πC$_1$ = C$_2$—π* N$_2$-C$_3$	33.73	0.24	0.085	33.66	0.24	0.085	36.88 (36.41)	0.23 (0.23)	0.086 (0.086)
6($\pi_{C=C}$—$\pi^*_{C=C}$)[a]	14.49–23.0			14.05–24.50			13.54–23.76		
LP(2)O—π* C$_6$-C$_{28}$	26.47	0.37	0.093	47.25	0.31	0.115			
LP(3)O—π* C$_6$-C$_7$	12.68	0.43	0.069	1.34	0.46	0.023	56.62 (56.53)	0.29	0.120

[a] There are six $\pi_{C=C}$–$\pi^*_{C=C}$ interactions with second-order perturbation energies between the two values shown; note that the values of $E_j - E_i$ and $F(i,j)$ are not shown for these interactions in order to keep the table relatively concise

[b] For the nonsymmetrical complex **3**, two values of each parameter are shown for each donor–acceptor interaction, the first for the atom of ligand 1 (O$_1$ or N$_1$) and the second (in parentheses) for the atom of ligand 2 (O$_2$ or N$_2$)
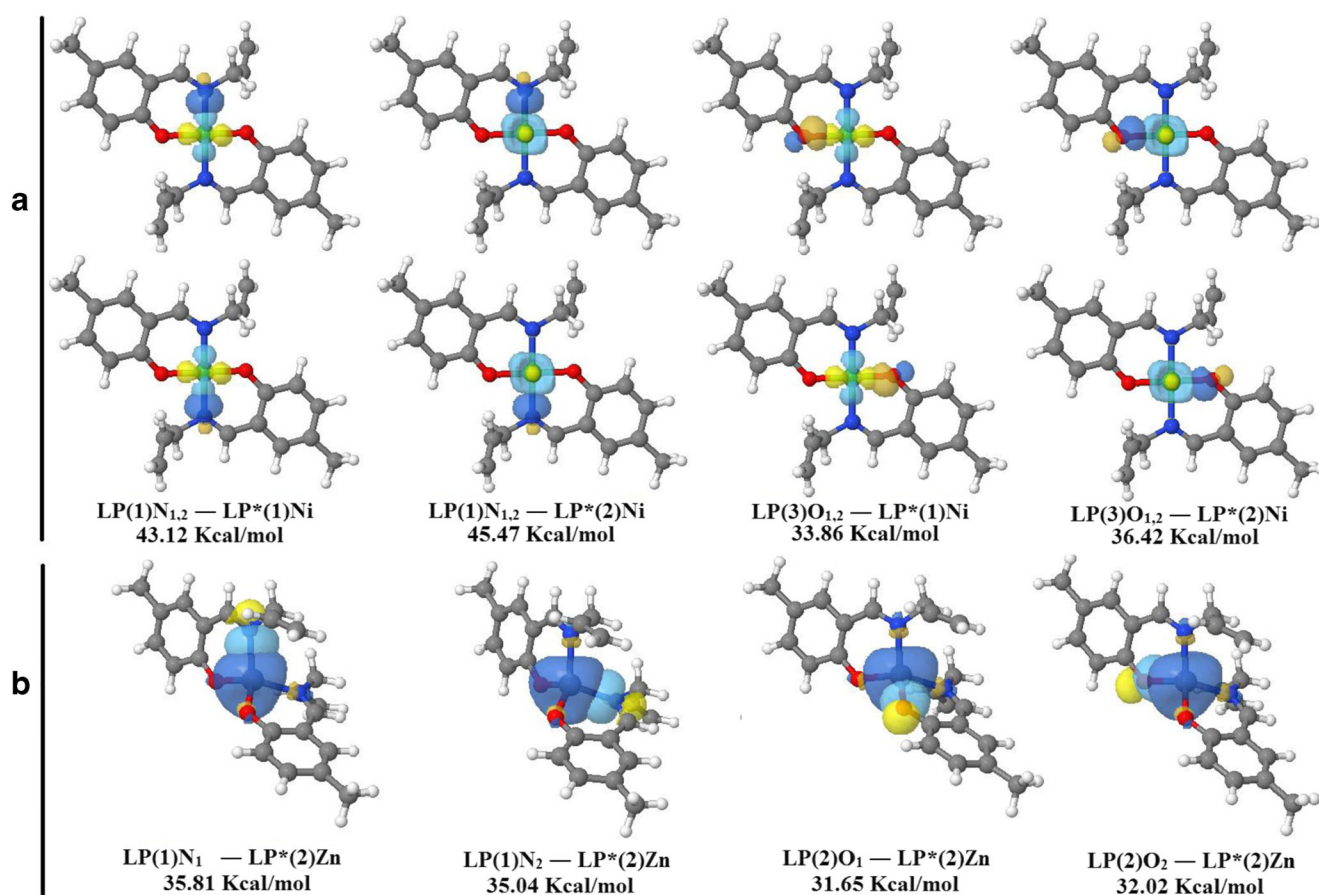
Fig. 2a–b Visualization of selected NBO–NBO* interactions in the complexes NiL_2^2 (**a**) and ZnL_2^2 (**b**), as calculated using B3LYP

Frontier molecular orbitals

The calculated frontier molecular orbital (FMO) energies and their compositions in terms of fragment orbitals in complexes **1** and **2** are given in Table 4 and Figure S2 of the ESM (the results obtained for complex **3** are given in Table S2 of the ESM). As reported in Table 4, the results obtained with the two functionals B3LYP and mPW1PW1 agree well in terms of the contributors to each molecular orbital, but their contributions differ depending on the functional used. The HOMOs of **1** and **2** are delocalized on the π^* orbital of the phenolate and include only a small contribution from metal d orbitals. The LUMOs of **1** and **2** are delocalized principally on the phenolate ring. The almost degenerate molecular orbitals H-2 and H-3 of A_g symmetry are mainly composed of $\pi_{phenolate}$ and metal d orbitals. The H-1, H-4, and H-5 molecular orbitals are mainly delocalized on the imine group and the phenolate ring of the ligand. The unoccupied molecular orbitals L+1 and L+2 are mixed orbitals ($\pi_{phenolate} + d_M$) with a considerable contribution from metal d orbitals, which leads to the possibility of d–d transitions. For complex **3**, the occupied d orbitals are lower in energy (H-7 to H-10 molecular orbitals). Indeed, the highest

occupied molecular orbitals (HOMO to H-5) and lowest unoccupied molecular orbitals (LUMO to L+10) are delocalized in the ligand orbitals. The computed energy gaps for complexes **1** and **2** are very similar and do not differ much from that of complex **3**. To study the effect of dimethylation of the phenolate rings in the ligands on the optical properties of the studied complexes, we studied the FMOs of the nickel complex without the two methyl groups on the phenolate rings (NiL_2^1; see Fig. S4 in the ESM). The calculated energies and compositions of the FMOs are given in Table S4 of the ESM. As shown in Tables 4 and S4 of the ESM, the dimethylation changes the FMO compositions slightly. Also note that the B3LYP-calculated energy gaps for NiL_2^1 (3.745 eV) and NiL_2^2 (3.679 eV) barely differ (the difference is only ~0.066 eV). We studied the effect of dimethylation only on the nickel complex, but we confidently predict that dimethylation of the zinc and palladium complexes will have the same effect.

TD-DFT study

The energies, oscillator strengths, and character of vertical transitions to low-lying singlet excited states of the complexes

Table 4 Energies, symmetries, and character of the FMOs of the complexes NiL_2^2 (**1**) and PdL_2^1 (**2**)

		B3LYP		mPW1PW91	
	Symmetry	ε (eV)	Character (%)	ε (eV)	Character (%)
NiL_2^2 (**1**)					
L+4	A_u	0.030	50% $\pi^\star_{allyl}$ + 46% $\pi^\star_{phenolate}$	0.243	74% $\pi^\star_{phenolate}$ + 24% $\pi^\star_{allyl}$
L+3	A_g	−0.057	51% $\pi^\star_{phenolate}$ + 44% $\pi^\star_{allyl}$	0.140	58% $\pi^\star_{phenolate}$ + 32% $\pi^\star_{allyl}$
L+2	A_u	−1.635	35% d_{Ni} + 62% $\pi^\star_{phenolate}$	−1.304	57% d_{Ni} + 40% $\pi^\star_{phenolate}$
L+1	A_g	−1.798	65% $\pi^\star_{phenolate}$ + 32% d_{Ni}	−1.622	77% $\pi^\star_{phenolate}$ + 20% d_{Ni}
LUMO	A_u	−1.814	97% $\pi^\star_{phenolate}$	−1.655	97% $\pi^\star_{phenolate}$
$\Delta\varepsilon$		3.679		4.097	
HOMO	A_g	−5.493	85% $\pi_{phenolate}$ + 14% d_{Ni}	−5.752	87% $\pi_{phenolate}$ + 12% d_{Ni}
H-1	A_g	−5.975	97% $\pi_{phenolate}$	−6.224	97% $\pi_{phenolate}$
H-2	A_g	−6.616	48% d_{Ni} + 49% $\pi_{phenolate}$	−7.017	38% d_{Ni} + 59% $\pi_{phenolate}$
H-3	A_g	−6.704	40% d_{Ni} + 58% $\pi_{phenolate}$	−7.087	83% d_{Ni} + 16% $\pi_{phenolate}$
H-4	A_u	−7.068	96% $\pi_{phenolate}$	−7.354	96% $\pi_{phenolate}$
H-5	A_g	−7.245	53% $\pi_{phenolate}$ + 46% π_{allyl}	−7.539	52% π_{allyl} + 48% $\pi_{phenolate}$
PdL_2^1 (**2**)					
L+4	A_g	−0.089	94% $\pi^\star_{phenolate}$	0.107	96% $\pi^\star_{phenolate}$
L+3	A_g	−0.163	77% $\pi^\star_{phenolate}$ + 20% $\pi^\star_{allyl}$	0.027	80% $\pi^\star_{phenolate}$
L+2	A_g	−1.708	83% $\pi^\star_{phenolate}$ + 13% d_{Pd}	−1.461	44% d_{Pd} + 53% $\pi^\star_{phenolate}$
L+1	A_u	−1.873	46% d_{Pd} + 51% $\pi^\star_{phenolate}$	−1.630	81% $\pi^\star_{phenolate}$ + 15% d_{Pd}
LUMO	A_g	−1.928	97% $\pi^\star_{phenolate}$	−1.795	97% $\pi^\star_{phenolate}$
$\Delta\varepsilon$		3.693		4.081	
HOMO	A_u	−5.621	82% $\pi_{phenolate}$ + 17% d_{Pd}	−5.876	83% $\pi_{phenolate}$ + 16% d_{Pd}
H-1	A_g	−6.158	97% $\pi_{phenolate}$	−6.428	97% $\pi_{phenolate}$
H-2	A_u	−6.727	79% d_{Pd} + 21% $\pi_{phenolate}$	−7.054	37% d_{Pd} + 60% $\pi_{phenolate}$
H-3	A_g	−6.779	36% d_{Pd} + 61% $\pi_{phenolate}$	−7.104	73 d_{Pd} + 26% $\pi_{phenolate}$
H-4	A_u	−7.181	94% $\pi_{phenolate}$	−7.475	93% $\pi_{phenolate}$
H-5	A_g	−7.412	60% π_{allyl} + 40% $\pi_{phenolate}$	−7.703	66% π_{allyl} + 33% $\pi_{phenolate}$

NiL_2^2 and PdL_2^1 in methanol, computed using B3LYP and mPW1PW91, are reported in Tables 5 and 6. For the complexes ZnL_2^2 and NiL_2^1, the results are reported in Tables S3 and S5 of the ESM. Simulated and observed electronic spectra of the studied complexes are depicted in Figs. 3, 4, and 5. The simulated absorption spectra of **1**–**3** reproduce the main characteristics of the corresponding experimental spectra. B3LYP redshifts the mPW1PW1 spectra of the three complexes, leading to better agreement with the observed absorptions in the blue region. Complexes **1** and **2** start to absorb at ~465 nm (B3LYP), ~440 nm (mPW1PW91), and ~465 nm (observed), whereas complex **3** starts to absorb at ~424 nm (B3LYP), ~411 nm (mPW1PW91), and ~427 nm (observed). This difference occurs because the energy gaps of the three complexes are different sizes. As shown in the Fig. 3, the complexes NiL_2^2 and NiL_2^1 present similar spectra. The complex NiL_2^1 starts to absorb at ~440 nm (B3LYP), which shows that dimethylation redshifts the spectrum in the visible region.

All transitions from S_0 to any singlet excited state with A_g symmetry are forbidden ($f = 0$) and were therefore omitted. To determine the character of the absorptions $S_0 \rightarrow S_n$, we analyzed the natural orbital transitions of the main excited singlet states of the three studied complexes (Fig. 6). The NTOs of the complexes **1**, **2**, and **3** are given in Fig. 6 and Fig. S3 of the ESM. This analysis is very useful for visualizing and identifying the nature of the electronic excitation associated with each absorption. The low-lying singlet excited states of the nickel and palladium complexes are mainly characterized by mixed charge transfer (LLCT, MLCT, and LMCT). In the zinc complex, pure LLCT is dominant. The transition $S_0 \rightarrow S_5$ in complex **1**, calculated using B3LYP to lead to absorption at 400 nm ($f = 0.078$), can be assigned to the weak band observed experimentally at around ~380 nm. The hole NTOs of this absorption are mainly composed of d_{Ni} and $\pi_{phenolate}$ orbitals, while the electron NTOs are delocalized over the $\pi^\star_{phenolate}$ orbital.

Table 5 Energies, oscillator strengths, and character of the main absorptions of the complex NiL_2^2 (**1**), as computed with mPW1PW91 and B3LYP

mPW1PW91						B3LYP					
State	Symmetry	λ (nm)	f > 0.09	Transition	Character	State	Symmetry	λ (nm)	f > 0.07	Transition	Character
S_5	A_u	376	0.109	HOMO → LUMO (95%)	LLCT/MLCT	S_5	A_u	400	0.078	HOMO → L+1 (96%)	LLCT/MLCT
S_{10}	A_u	311	0.095	H-1 → L+1 (51%) H-1 → L+2 (45%)	LLCT/LMCT	S_{10}	A_u	330	0.104	H-1 → LUMO (28%) H-1 → L+2 (68%)	LLCT/LMCT
S_{13}	A_u	274	0.369	H-3 → LUMO (19%) H-2 → LUMO (72%)	MLCT/LLCT	S_{13}	A_u	292	0.266	H-3 → L+1 (89%)	MLCT/LLCT
S_{19}	A_u	248	0.250	H-7 → LUMO (16%) H-6 → LUMO (33%) H-5 → L+1 (12%) H-5 → L+2 (14%)	LLCT/LMCT	S_{19}	A_u	264	0.214	H-6 → L+1 (48%) H-5 → L+2 (21%)	LLCT/MLCT
S_{21}	A_u	243	0.223	H-7 → LUMO (25%) H-5 → L+2 (11%) H-4 → L+2 (17%) HOMO → L+3 (30%)	LMCT/LLCT/MLCT	S_{21}	A_u	259	0.299	H-7 → L+1 (18%) H-6 → L+1 (19%) H-5 → L+2 (36%) HOMO→L+3 (14%)	LLCT/MLCT/LMCT/MC
S_{22}	A_u	243	0.499	H-6 → LUMO (39%) H-5 → L+2 (23%) H-4 → L+1 (17%)	LLCT/LMCT	S_{23}	A_u	255	0.121	H-7 → L+1 (31%) H-6 → L+1 (21%) H-5 → L+2 (11%) H-4 → L+2 (10%) HOMO → L+3 (13%)	LLCT/MLCT/LMCT/MC
S_{28}	A_u	231	0.395	HOMO → L+6 (76%)	MLCT/LLCT	S_{27}	A_u	251	0.100	H-5 → L+2 (10%) H-4 → LUMO (13%) H-4 → L+2 (33%) HOMO → L+3 (17%) HOMO → L+6 (18%)	LLCT/MLCT/LMCT/MC
S_{32}	A_u	226	0.171	H-9 → LUMO (16%) H-8 → L+1 (55%)	LLCT/LMCT/MLCT	S_{29}	A_u	244	0.345	H-8 → L+1 (15%) HOMO → L+6 (57%)	MLCT/LLCT
S_{38}	A_u	217	0.090	H-8 → L+2 (67%)	LLCT/MLCT	S_{32}	A_u	241	0.234	H-10 → L+1 (19%) H-8 → L+1 (53%) HOMO → L+6 (10%)	LLCT/MLCT
S_{45}	A_u	207	0.619	H-1 → L+4 (14%) H-1 → L+5 (21%) HOMO → L+8 (17%) HOMO → L+9 (32%)	LLCT	S_{35}	A_u	236	0.125	H-10 → L+1 (56%) H-8 → L+1 (16%)	LLCT/MLCT
						S_{38}	A_u	230	0.148	H-9 → L+2 (18%) HOMO→L+7 (71%)	LLCT/LMCT/MC/MLCT
						S_{44}	A_u	216	0.507	H-1 → L+5 (17%) HOMO → L+8 (58%)	LLCT/LMCT/MLCT/MC

Table 6 Energies, oscillator strengths, and character of the main absorptions of the complex PdL_2^1 (2), as computed with mPW1PW91 and B3LYP

mPW1PW91

State	Symmetry	λ (nm)	f > 0.09	Transition	Character
S3	A_u	382	0.091	HOMO → LUMO(96%)	LLCT/MLCT
S9	A_u	301	0.091	H-1 → L+1 (53%) H-1 → L+2 (41%)	LLCT/LMCT
S12	A_u	276	0.421	H-3 → LUMO (22%) H-2 → LUMO (70%)	MLCT/LLCT
S19	A_u	246	0.129	H-6 → LUMO (16%) H-5 → L+1 (53%) HOMO → L+3 (10%)	LLCT/LMCT/MLCT
S22	A_u	239	0.346	H-7 → LUMO (58%) H-5 → L+2 (15%) HOMO → L+3 (15%)	LLCT/LMCT/MLCT/MC
S23	A_u	235	0.634	H-7 → LUMO (17%) H-5 → L+2 (27%) H-4 → L+1 (22%) H-4 → L+2 (14%)	LLCT/LMCT/MLCT/MC
S28	A_u	229	0.118	H-9 → LUMO (20%) HOMO → L+6 (61%)	MLCT/LLCT
S31	A_u	228	0.228	H-9 → LUMO (35%) H-8 → L+1 (22%) HOMO → L+6 (17%)	MLCT/LMCT/MLCT/MC
S34	A_u	222	0.126	H-10 → LUMO (21%) H-8 → L+1 (22%) H-5 → L+2 (15%) HOMO → L+7 (20%)	LLCT/LMCT
S37	A_u	216	0.358	H-8 → L+2 (39%) HOMO → L+7 (32%)	LLCT/MLCT
S45	A_u	202	0.344	H-1 → L+4 (18%) H-1 → L+5 (10%) HOMO → L+8 (46%)	LLCT/MLCT/LMCT/MC

B3LYP

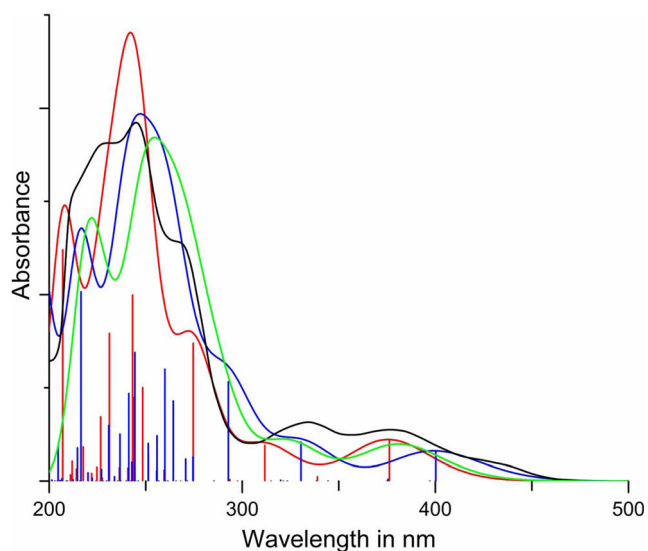| State	Symmetry	λ (nm)	f > 0.06	Transition	Character
S3	A_u	404	0.069	HOMO → LUMO (97%)	LLCT/MLCT
S9	A_u	319	0.089	H-1 → L+2 (87%)	LLCT/LMCT
S12	A_u	291	0.333	H-3 → LUMO (86%)	LLCT/MLCT
S19	A_u	259	0.242	H-5 → L+1 (63%) HOMO → L+3 (12%)	LLCT/LMCT/MLCT
S23	A_u	253	0.146	H-7 → LUMO (41%) H-5 → L+2 (27%) HOMO → L+3 (18%)	LLCT/MLCT
S24	A_u	250	0.158	H-7 → LUMO (15%) H-5 → L+1 (20%) H-5 → L+2 (35%)	LLCT/MLCT
S25	A_u	247	0.121	H-4 → L+2 (41%) HOMO → L+3 (16%) HOMO → L+6 (29%)	LLCT/LMCT/MLCT
S29	A_u	243	0.657	H-8 → L+1 (16%) H-4 → L+2 (19%) HOMO → L+6 (47%)	LLCT/LMCT
S31	A_u	241	0.075	H-9 → LUMO (44%) H-8 → L+1 (31%)	
S34	A_u	233	0.093	H-10 → LUMO (26%) H-8 → L+2 (40%) H-5 → L+2 (12%)	LLCT/MLCT
S35	A_u	232	0.061	H-10 → LUMO (58%) H-8 → L+2 (22%)	
S37	A_u	228	0.470	HOMO → L+7 (66%)	
S45	A_u	211	0.294	H-3 → L+3 (11%) H-1 → L+4 (13%) HOMO → L+8 (47%) HOMO → L+9 (15%)	LLCT/MLCT

Fig. 3 Simulated absorption spectra (*solid lines*) and calculated absorptions (*bars*) of the complex NiL_2^2 (**1**), as obtained using B3LYP (*blue*) and mPW1PW91 (*red*). Also shown is the simulated absorption spectrum of the complex NiL_2^1 (**4**), obtained using B3LYP (*green line*), and the digitized experimental spectrum from [12] (*black line*)
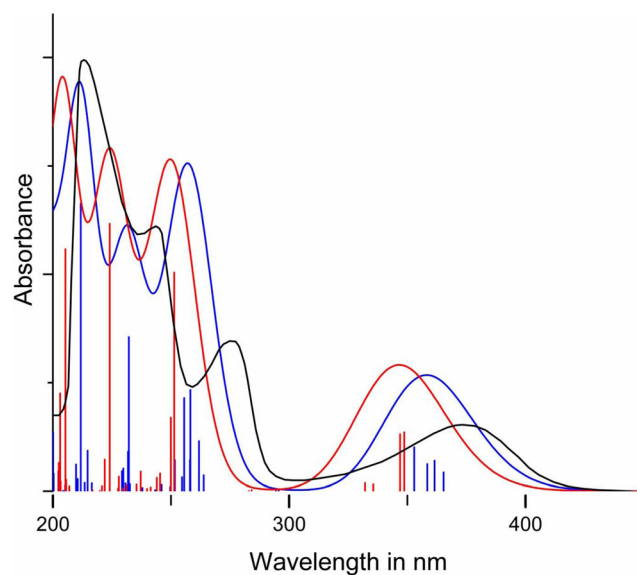

Fig. 5 Simulated absorption spectra (*solid lines*) and calculated absorptions (*bars*) of the complex ZnL_2^2 (**3**), as obtained using B3LYP (*blue*) and mPW1PW91 (*red*). Also shown is the digitized experimental spectrum from [12] (*black line*)

The weak band and shoulder observed at ~330 nm and ~268 nm, respectively, in the spectrum of complex **1** can be assigned to the two absorptions $S_0 \rightarrow S_{10}$ ($f = 0.104$) and $S_0 \rightarrow S_{19}$ ($f = 0.214$), which are calculated to occur at 330 nm and 264 nm, respectively, using B3LYP. In the ultraviolet C region, the intense band observed at ~245 nm is assigned to a set of excited states calculated to occur in the interval 264–231 nm, in particular the S_{29} state, which is
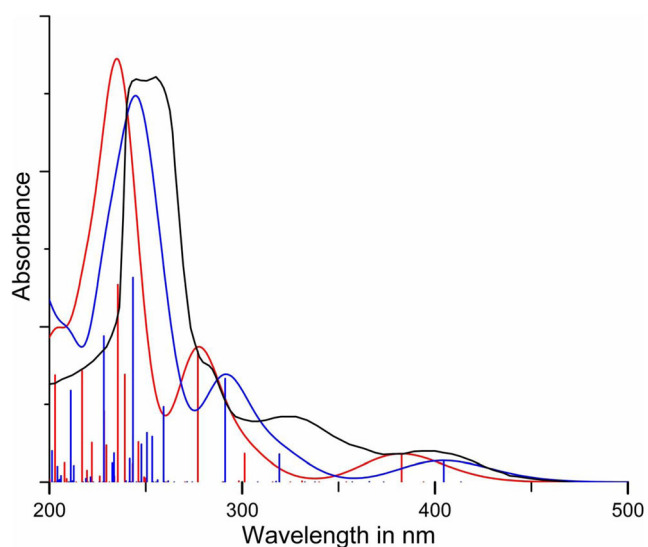

Fig. 4 Simulated absorption spectra (*solid lines*) and calculated absorptions (*bars*) of the complex PdL_2^1 (**2**), as obtained using B3LYP (*blue*) and mPW1PW91 (*red*). Also shown is the digitized experimental spectrum from [12] (*black line*)

calculated to occur at 244 nm with a strong oscillator strength $f = 0.345$. NTO analyzes show that this absorption ($S_0 \rightarrow S_{29}$) corresponds to two donor–acceptor pairs: the predominant donation occurs from d_{Pd} and $\pi_{phenolate}$ orbitals to the $\pi^\star_{phenolate}$ orbital, while the other donation mainly occurs via the $\pi_{phenolate} \rightarrow \pi^\star_{phenolate}$ transition. For complex **2**, the two absorptions $S_0 \rightarrow S_3$ (404 nm, $f = 0.069$) and $S_0 \rightarrow S_9$ (319 nm, $f = 0.089$) computed using B3LYP are assigned to two weak bands observed at 396 nm and 324 nm, respectively. The shoulder observed at ~280 nm can be assigned to the absorption $S_0 \rightarrow S_{19}$, which corresponds to a transition from d_{Pd} and $\pi_{phenolate}$ orbitals (the hole) to $\pi^\star_{phenolate}$ orbitals (the electron). At the highest energies, the most intense of the observed bands can be assigned to the intense B3LYP-calculated absorption $S_0 \rightarrow S_{29}$ ($f = 0.657$) at 243 nm, which mostly corresponds to the transition $\pi_{phenolate} \rightarrow \pi^\star_{phenolate}$, although the transition $d_{Pd} \rightarrow \pi^\star_{phenolate}$ also plays a role according to the NTO analysis (Fig. 6). For complex **3**, the weak band observed at 370 nm is assigned to the four absorptions calculated to occur in the interval 365–352 nm ($0.043 < f < 0.101$), which correspond to $\pi_{phenolate} \rightarrow \pi^\star_{phenolate}$ transitions. In the UV region, the two bands observed at ~275 nm (moderately intense) and ~212 nm (intense) are mainly assigned to the two absorptions $S_0 \rightarrow S_9$ (258 nm, $f = 0.233$) and $S_0 \rightarrow S_{28}$ (211 nm, $f = 0.663$), which correspond to pure ligand-to-ligand charge transfer. In the same region, the band observed at ~243 nm can be assigned to the $S_0 \rightarrow S_{20}$ transition, computed to occur at 232 nm, which has mixed (LLCT/MLCT) character.

Fig. 6 Natural orbital transitions and their eigenvalues for the main excited singlet states of the complexes NiL_2^2 (**1**) and PdL_2^1 (**2**), as calculated with B3LYP
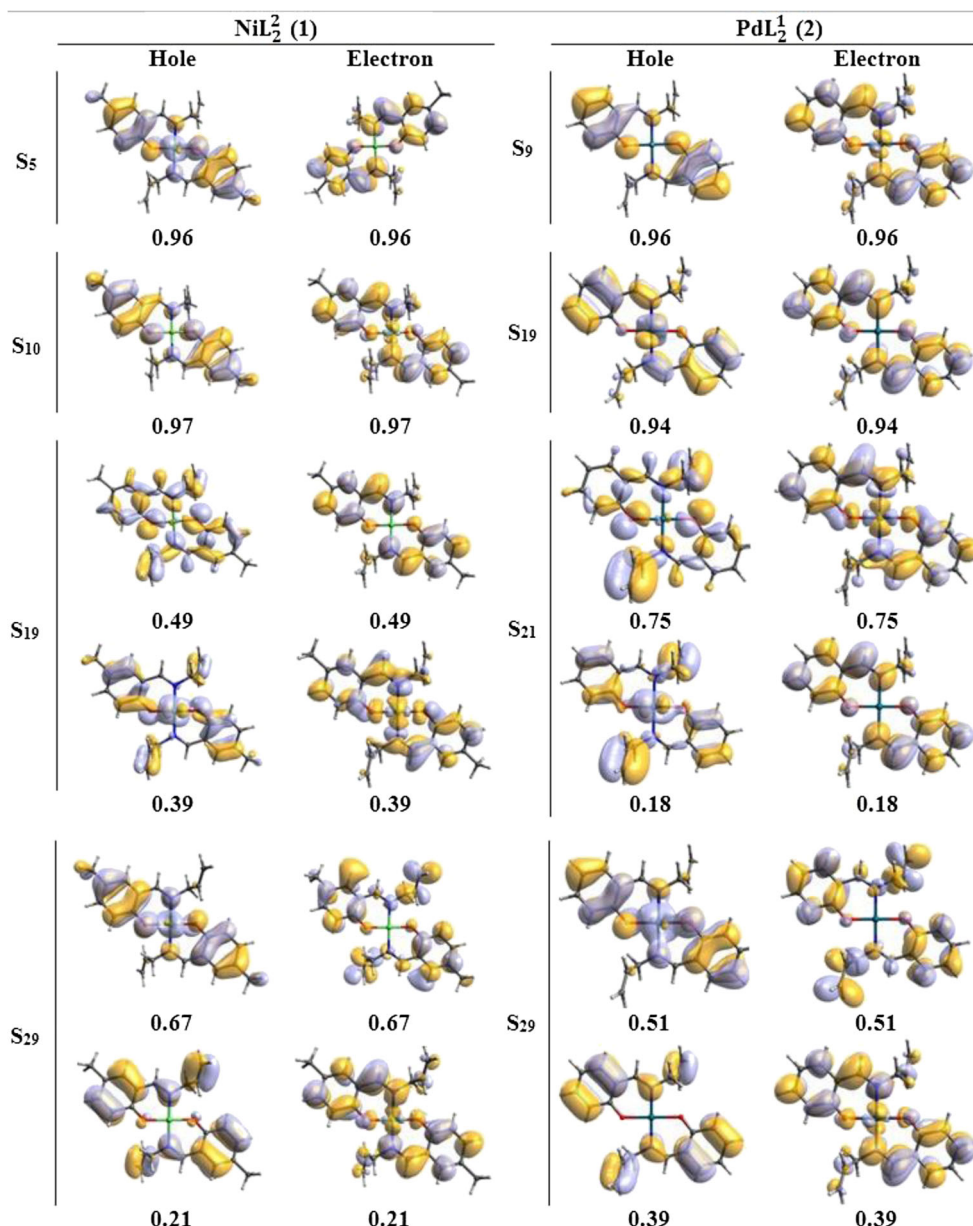
Conclusions

In this study, the geometric parameters, natural bond orbitals, frontier molecular orbitals, and electronic absorption spectra of complexes **1–3** were calculated using DFT and TD-DFT methods. The geometric parameters computed using B3LYP and mPW1PW91 were found to be in good agreement with the corresponding experimental data. Wiberg bond indices indicated that the metal–N and metal–O bonds in these complexes are only weakly covalent. NBO analysis showed that in complexes **1** and **2**, the metal ion coordinates to nitrogen and oxygen atoms through electron donation from lone pairs on the nitrogen and oxygen atoms to s and d orbitals on the metal ion; the energy (E^2) associated with this coordination is

significant. In complex **3**, the coordination occurs through electron donation from nitrogen and oxygen orbitals to s orbitals on the metal ion. FMO analysis showed that the occupied and unoccupied orbitals of complexes **1**, **2**, and **4** are globally delocalized in the $\pi_{phenolate}$ orbitals, with a significant proportion of the metal d orbitals contributing to some of the frontier molecular orbitals. For complex **3**, the frontier molecular orbitals are generally delocalizied in the ligand orbitals. The simulated absorption spectra of **1–3** presented similar shapes to the corresponding observed spectra. The B3LYP-calculated spectra of the three complexes showed better agreement with the observed absorptions in the blue region than the mPW1PW91-calculated spectra did. Dimethylation of the two phenolate ligands was calculated to redshift the spectrum of

the nickel complex; the same behavior is probably exhibited by the other complexes. The low-lying singlet excited states of complexes **1** and **2** have mixed (LLCT/MLCT/LMCT) charge-transfer character, while those of complex **3** have pure LLCT character. Intense bands observed in the absorption spectra for complexes **1** and **2** were assigned to the transitions $\pi_{phenolate} \rightarrow \pi^{\star}_{phenolate}$ and $d_{Metal} \rightarrow \pi^{\star}_{phenolate}$. For complex **3**, an intense band observed in the UV region was assigned to pure ligand-to-ligand charge transfer.

References

1. Amiri Rudbari H, Riahi Farsani M, Lanza S, Bruno G, Yadollahi B (2015) Chirality at octahedral centres determined by tetradentate Schiff base ligands. C R Chim 18:391–398. https://doi.org/10.1016/j.crci.2014.06.002

2. Chakraborty S, Bhattacharjee CR, Mondal P, Prasad SK, Rao DSS (2015) Synthesis and aggregation behaviour of luminescent meso-morphic zinc(II) complexes with 'salen' type asymmetric Schiff base ligands. Dalton Trans 44:7477–7488. https://doi.org/10.1039/c4dt03989k

3. Rezaeivala M, Keypour H (2014) Schiff base and non-Schiff base macrocyclic ligands and complexes incorporating the pyridine moiety—the first 50 years. Coord Chem Rev 280:203–253. https://doi.org/10.1016/j.ccr.2014.06.007

4. Wu F, Wang C-J, Lin H, Jia A-Q, Zhang Q-F (2018) Syntheses, structures and catalytic properties of ruthenium(II) nitrosyl complexes with bidentate and tetradentate Schiff base ligands. Inorg Chim Acta 471:718–723. https://doi.org/10.1016/j.ica.2017.12.004

5. Ajlouni AM, Abu-Salem Q, Taha ZA, Hijazi AK, Al Momani W (2016) Synthesis, characterization, biological activities and luminescent properties of lanthanide complexes with [2-thiophenecarboxylic acid, 2-(2-pyridinylmethylene)hydrazide] Schiff bases ligand. J Rare Earths 34:986–993. https://doi.org/10.1016/s1002-0721(16)60125-4

6. Keypour H, Shooshtari A, Rezaeivala M, Mohsenzadeh F, Rudbari HA (2015) Synthesis and characterization of transition metal complexes of a hexadentate N_4O_2 donor Schiff base ligand: X-ray crystal structures of the copper(II) and zinc(II) complexes and their antibacterial properties. Transition Met Chem (London) 40:715–722. https://doi.org/10.1007/s11243-015-9966-6

7. Mahapatra DK, Das D, Shivhare R (2017) Substituted thiazole linked murrayanine-Schiff's base derivatives as potential anti-breast cancer candidates: future EGFR kinase inhibitors. Int J Pharm Sci Drug Res 9:139–144. https://doi.org/10.25004/ijpsdr.2017.090307

8. Sun WH, Li KH, Liu H, Gu YT, Zhang Y, You ZL, Li W (2017) Synthesis, characterization, crystal structures, and antibacterial activity of polynuclear nickel(II) and copper(II) complexes with similar tridentate Schiff bases. Russ J Coord Chem 43:693–699. https://doi.org/10.1134/s1070328417100104

9. Khorshidifard M, Amiri Rudbari H, Kazemi-Delikani Z, Mirkhani V, Azadbakht R (2015) Synthesis, characterization and X-ray crystal structures of vanadium(IV), cobalt(III), copper(II) and zinc(II) complexes derived from an asymmetric bidentate Schiff-base ligand at ambient temperature. J Mol Struct 1081:494–505. https://doi.org/10.1016/j.molstruc.2014.10.071

10. Majumder S, Bhattacharya A, Naskar JP, Mitra P, Chowdhury S (2013) An oxorhenium(V) Schiff-base complex: synthesis, characterisation, structure, spectroscopic and electrochemical aspects. Inorg Chim Acta 399:166–171. https://doi.org/10.1016/j.ica.2013.01.018

11. Poulter N, Donaldson M, Mulley G, Duque L, Waterfield N, Shard AG, Spencer S, Jenkins ATA, Johnson AL (2011) Plasma deposited metal Schiff-base compounds as antimicrobials. New J Chem 35:1477. https://doi.org/10.1039/c1nj20091g

12. Amiri Rudbari H, Iravani MR, Moazam V, Askari B, Khorshidifard M, Habibi N, Bruno G (2016) Synthesis, characterization, X-ray crystal structures and antibacterial activities of Schiff base ligands derived from allylamine and their vanadium(IV), cobalt(III), nickel(II), copper(II), zinc(II) and palladium(II) complexes. J Mol Struct 1125:113–120. https://doi.org/10.1016/j.molstruc.2016.06.055

13. Devi N, Sarma K, Rahaman R, Barman P (2018) Synthesis of a new series of Ni(II), Cu(II), Co(II) and Pd(II) complexes with an ONS donor Schiff base: crystal structure, DFT study and catalytic investigation of palladium and nickel complexes towards deacylative sulfenylation of active methylenes and regioselective 3-sulfenylation of indoles via thiouronium salt formation. Dalton Trans 47:4583–4595. https://doi.org/10.1039/c7dt04635a

14. Mahmoud WH, Deghadi RG, Mohamed GG (2018) Metal complexes of novel Schiff base derived from iron sandwiched organometallic and 4-nitro-1,2-phenylenediamine: synthesis, characterization, DFT studies, antimicrobial activities and molecular docking. Appl Organomet Chem 32:e4289. https://doi.org/10.1002/aoc.4289

15. Salehi M, Faghani F, Kubicki M, Bayat M (2018) New complexes of Ni(II) and Cu(II) with tridentate ONO Schiff base ligand: synthesis, crystal structures, electrochemical and theoretical investigation. J Iran Chem Soc 15:2229–2240. https://doi.org/10.1007/s13738-018-1412-1

16. Becke AD (1993) Density-functional thermochemistry. III. The role of exact exchange. J Chem Phys 98:5648. https://doi.org/10.1063/1.464913

17. Hohenberg P, Kohn W (1964) Inhomogeneous electron gas. Phys Rev 136:B864–B871. https://doi.org/10.1103/physrev.136.b864

18. Lee C, Yang W, Parr RG (1988) Development of the Colle–Salvetti correlation-energy formula into a functional of the electron density. Phys Rev B 37:785–789. https://doi.org/10.1103/physrevb.37.785

19. Adamo C, Barone V (1998) Exchange functionals with improved long-range behavior and adiabatic connection methods without adjustable parameters: the mPW and mPW1PW models. J Chem Phys 108:664. https://doi.org/10.1063/1.475428

20. Binning RC, Curtiss LA (1990) Compact contracted basis sets for third-row atoms: Ga–Kr. J Comput Chem 11:1206–1216. https://doi.org/10.1002/jcc.540111013

21. Krishnan R, Binkley JS, Seeger R, Pople JA (1980) Self-consistent molecular orbital methods. XX. A basis set for correlated wave functions. J Chem Phys 72:650. https://doi.org/10.1063/1.438955

22. McLean AD, Chandler GS (1980) Contracted Gaussian basis sets for molecular calculations. I. Second row atoms, Z=11–18. J Chem Phys 72:5639. https://doi.org/10.1063/1.438980

23. Hay PJ, Wadt WR (1985) Ab initio effective core potentials for molecular calculations. Potentials for the transition metal atoms Sc to Hg. J Chem Phys 82:270. https://doi.org/10.1063/1.448799

24. Hay PJ, Wadt WR (1985) Ab initio effective core potentials for molecular calculations. Potentials for K to Au including the outermost core orbitals. J Chem Phys 82:299. https://doi.org/10.1063/1.448975

25. Cancès E, Mennucci B, Tomasi J (1997) A new integral equation formalism for the polarizable continuum model: theoretical background and applications to isotropic and anisotropic dielectrics. J Chem Phys 107:3032. https://doi.org/10.1063/1.474659

26. Cossi M, Barone V, Mennucci B, Tomasi J (1998) Ab initio study of ionic solutions by a polarizable continuum dielectric model. Chem Phys Lett 286:253–260. https://doi.org/10.1016/s0009-2614(98)00106-7

27. Brahim H, Haddad B, Boukabene M, Brahim S, Ariche B (2017) Theoretical study of geometric structures and electronic absorption spectra of iridium(III) complexes based on 2-phenyl-5-nitropyridyl with different ancillary ligands. Comput Theor Chem 1101:8–19. https://doi.org/10.1016/j.comptc.2016.12.016

28. Brahim H, Haddad B, Brahim S, Guendouzi A (2017) DFT/TDDFT computational study of the structural, electronic and optical properties of rhodium(III) and iridium(III) complexes based on tris-picolinate bidentate ligands. J Mol Model 23:344. https://doi.org/10.1007/s00894-017-3517-3

29. Foster JP, Weinhold F (1980) Natural hybrid orbitals. J Am Chem Soc 102:7211–7218. https://doi.org/10.1021/ja00544a007

30. Reed AE, Weinhold F (1983) Natural bond orbital analysis of near-Hartree–Fock water dimer. J Chem Phys 78:4066–4073. https://doi.org/10.1063/1.445134

31. Reed AE, Weinhold F (1985) Natural localized molecular orbitals. J Chem Phys 83:1736–1740. https://doi.org/10.1063/1.449360

32. Reed AE, Weinstock RB, Weinhold F (1985) Natural population analysis. J Chem Phys 83:735–746. https://doi.org/10.1063/1.449486

33. Weinhold F, Landis CR (2001) Natural bond orbitals and extensions of localized bonding concepts. Chem Educ Res Pract 2:91–104. https://doi.org/10.1039/b1rp90011k

34. Glendening ED, Badenhoop JK, Reed AE, Carpenter JE, Bohmaann JA, Morales CM, Weinhold F (2001) NBO. Theoretical Chemistry Institute, University of Wisconsin, Madison

35. Frisch MJ, Trucks GW, Schlegel HB, Scuseria GE, Robb MA, Cheeseman JR, Scalmani G, Barone V, Mennucci B, Petersson GA, Nakatsuji H, Caricato M, Li X, Hratchian HP, Izmaylov AF, Bloino J, Zheng G, Sonnenberg JL, Hada M, Ehara M, Toyota K, Fukuda R, Hasegawa J, Ishida M, Nakajima T, Honda Y, Kitao O, Nakai H, Vreven T, Montgomery Jr JA, Peralta JE, Ogliaro F, Bearpark M, Heyd JJ, Brothers E, Kudin KN, Staroverov VN, Kobayashi R, Normand J, Raghavachari K, Rendell A, Burant JC, Iyengar SS, Tomasi J, Cossi M, Rega N, Millam JM, Klene M, Knox JE, Cross JB, Bakken V, Adamo C, Jaramillo J, Gomperts R, Stratmann RE, Yazyev O, Austin AJ, Cammi R, Pomelli C, Ochterski JW, Martin RL, Morokuma K, Zakrzewski VG, Voth GA, Salvador P, Dannenberg JJ, Dapprich S, Daniels AD, Foresman JB, Ortiz JV, Cioslowski J, Fox DJ (2009) Gaussian 09. Gaussian, Inc., Wallingford

36. Jmol Development Team (2013) Jmol: an open-source Java viewer for chemical structures in 3D. http://www.jmol.org/

37. Patek M (2013) Jmol NBO Visualization Helper. http://www.marcelpatek.com/nbo/nbo.html. Accessed 2 Jul 2018

38. Deilami AB, Salehi M, Arab A, Amiri A (2018) Synthesis, crystal structure, electrochemical properties and DFT calculations of three new Zn(II), Ni(II) and Co(III) complexes based on 5-bromo-2-((allylimino)methyl)phenol Schiff-based ligand. Inorg Chim Acta 476:93–100 http://www.sciencedirect.com/science/article/pii/S0020169317316134